Station keeping of a subsea shuttle tanker system under extreme current during offloading

Yucong Ma, Terje Andreas Jevnaker & Yihan Xing

Published online: 15 May 2023.

Submit your article to this journal ⇗

Article views: 103

View related articles ⇗

View Crossmark data ⇗

Station keeping of a subsea shuttle tanker system under extreme current during offloading

Yucong Ma ⬢, Terje Andreas Jevnaker and Yihan Xing ⬢

Department of Mechanical and Structural Engineering and Materials Science, University of Stavanger, Stavanger, Norway

ABSTRACT

This paper presents the station keeping challenge of the subsea shuttle tanker (SST) design during underwater loading and offloading at a subsea well under an extreme current environment. The paper investigates the movement of the SST during offloading with extreme current speeds, i.e. above 1.6 m/s, in the surge, heave and pitch motions, respectively. A linear quadratic regulator (LQR) is used for SST motion control. The LQR's primary focus is to achieve the target for the SST during the offloading process. Then, the average exceedance rate method is used to predict the maximum and minimum potential depth excursion. This extreme value prediction result will serve as a basis for obtaining a cost-efficient design of the subsea shuttle tanker and provide recommendations for the decision-makers upon SST operation.

1. Introduction

1.1. Subsea shuttle tanker

Oil and gas production in the offshore environment has been evolving rapidly since the first offshore well was drilled in the Gulf of Mexico in 1947 (Bai and Bai 2018). Subsea pipelines and tanker ships have been utilised to transport the produced oil and gas from the offshore subsea fields to onshore facilities for refinement and delivery to the end consumer. However, technical and economic restrictions limit the applications of such transportation methods in some scenarios. The field development cost of submarine pipelines is directly proportional to the transportation distance and inflates with the growth of water depth. Because of this, submarine pipelines are commonly installed for fields with large annuity close to the coast and are not feasible for remote fields with low profit margins. In this situation, tanker ships are deployed. Tanker ships are more flexible and can be easily switched to other fields depending on the demand. Still, these vessels are dependent on environmental circumstances and cannot work in severe sea states. Considering all these limitations, a subsea shuttle tanker (SST) system is proposed as a possible weather-independent transportation method for remote marginal fields.

The SST concept (as illustrated in Figure 1) was first unveiled in two research disclosures by Equinor (Equinor Energy AS 2019; Ellingsen et al. 2020), in which multiple freight submersible concepts are proposed, such as train-like AUV, subsea glider, and SST. Xing et al. (2021a) focused on the SST concept and entailed the most critical design considerations of using civilian submersibles to transport liquid carbon dioxide. Based on these, a 34,000-tonne baseline design SST was presented by Ma et al. (2021). The baseline SST is an electric-propelled AUV with a liquid CO_2 capacity of 16,362 m^3, which can fulfil the annual need of any ongoing carbon capture and storage project in Norway.

The SST can help mitigate climate change and advance the industry towards net zero as it is electrically propelled and therefore has zero carbon footprint during transportation. This contributes to the maritime industry's sustainability, with roughly 3.3% of the CO_2 emission resulting from fossil fuels (Papanikolaou 2014). In addition, a technical-economic study found that the SST can become the enabler to the utilisation of subsea fields with an annual storage capacity below 2.5 million tonnes per annual for carbon storage projects (Xing et al. 2021b).

1.2. Offloading process

The unloading process of the SST is illustrated in Figure 2. The SST will first hover in the vicinity above the subsea well during this process. Then, a remotely operated vehicle (ROV) deployed at the subsea well launches and carries a flowline to mate with the SST. After the flowline is appropriately connected, the SST discharges CO_2 to the wellhead. Meanwhile, it pumps in seawater to ensure neutral buoyancy. Finally, the ROV disconnects with the SST when this process is finished. The entire offloading operation consumes 4 h. The SST is subjected to various environmental loads, as illustrated in Figure 3, such as hydrostatic pressure, wave loads in shallow water, and ocean current.

Ocean current has the most considerable dynamic effects over the SST as it drives the vessel to an off-site away from its desired reference position. Therefore, the SST uses its hovering system consisting of a propeller and two thrusters to cope with the ocean current load. Smaller AUV designs often utilise vertical propellers or vertical ballast systems for accurate hovering control (Zhao et al. 2016). Though the ballast system can account for weight change during offloading, the thrusters will accommodate actuation at higher frequencies.

A comprehensive understanding of the motion in extreme currents is vital to the SST design. As a previous study shows, the side-way current drag is 80 times greater than the heading current, and the SST has to constantly head-on current while offloading (Ma et al. 2022a; Ma et al. 2022b). When the SST is facing ocean current, the surge off-site affects the required designed length of the flowline to avoid tautly and snap loads. The ocean current can also
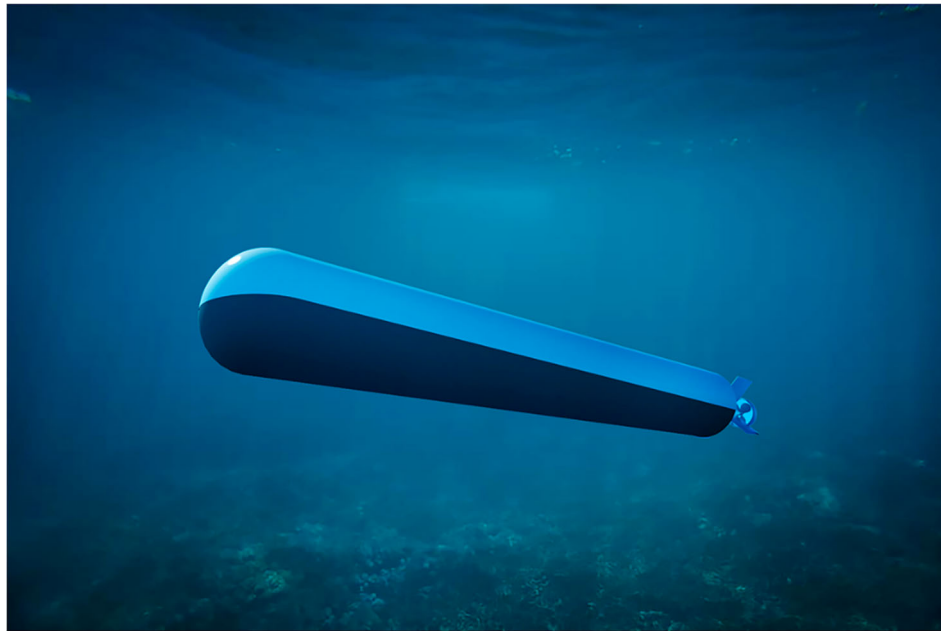
Figure 1. Subsea shuttle tanker illustration. (This figure is available in colour online.)
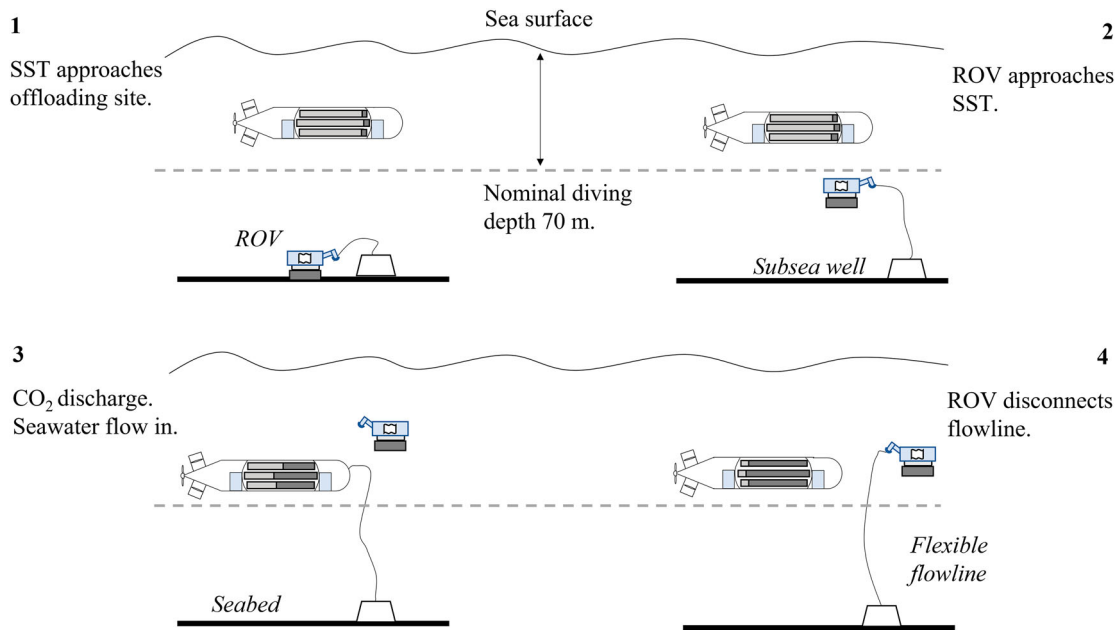

Figure 2. Subsea shuttle tanker unloading sequence. (This figure is available in colour online.)
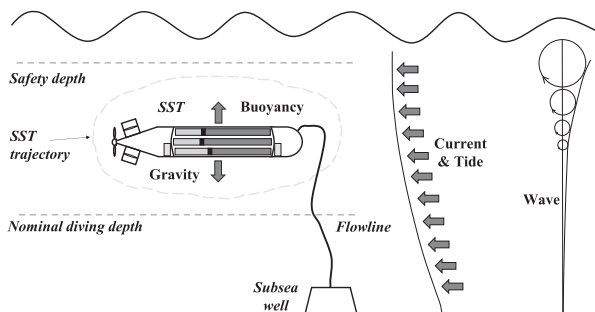

Figure 3. Environmental loads that act on the SST during offloading. (This figure is available in colour online.)

result in severe heave and pitch motions. This decides the maximum depth excursion of the SST, which determines the collapse pressure and is the dominating factor of the SST pressure hull design. The baseline SST applies the state-of-the-art engineering code (DNV 2018), which was commonly used on military submarines with heavy steel structures and closely arranged ring stiffeners. It suggested a high safety factor of 2.7 when determining the SST collapse pressure. However, as a merchant's vessel, it is essential for the SST to have an over 50% payload-over-displacement ratio to be economically feasible. Therefore, to reduce this safety factor, a throughout understanding of the nature of the SST manoeuvring is essential. This requires a consideration of all possible operation scenarios, environmental loads, and possible failure modes of the SST. The

surface environmental load, i.e. wind and wave effects, are reduced mainly as the SST travels at 70 m water depth. The wave-induced motions are expected to be slow and a few magnitudes more minor than the SST motions (Patel et al. 2023). In Ma and Xing (2022), the SST sailing operation is studied to identify the SST safety operational envelope (Burcher and Rydill 1994; Renilson 2018). The results suggest that with the current 19 bar (190 m depth) collapse pressure, the operational depth of the SST can be increased from 70 m to 110 m. Otherwise, the designed collapse pressure can be reduced correspondingly. This will potentially reduce structural weight and therefore increase the payload capacity. This work supports the design by looking into the extreme depth excursions during the other essential scenarios of the SST operation – offloading. The minimum depth excursion affects the safety depth of the SST during operation. It indicates the shallowest depth that the SST could ever reach during offloading. Knowing this is vital for the SST to avoid collision with large draught ships or other surface installations.

Currently, the authors do not know that any research or studies within control theory and hovering of AUVs with the proposed SST size in extreme current have been conducted. In an effort to close this knowledge gap, the paper utilises the state-of-the-art ACER method to predict the maximum displacement for the discretely sampled response process. Even though the control theory for autonomous subsea vehicles is already widely explored, its application to the AUV of this class is still left blank.

In this paper, the control and station keeping of the SST during the offloading process is studied using a linear quadratic regulator (LQR). The main findings will be used as a basis to optimise the baseline design cost-efficiently and provide suggestions for the operation of the SST. This process is presented in Figure 4. First, a non-linear planar manoeuvring model was proposed. After this, the SST planar model is linearised to a simplified state-space model, which again is used to determine the desired controller gain during offloading. Subsequently, a Luenberger observer measures the SST motion response due to current and disturbance and feeds it back into the LQR control for calculations of the control input. Ocean current is non-linear and changes with time and location. Modelling of the ocean current follows a Gauss-Markov process, presented by Fossen (2021) and Sørensen (2018), also employed by Ma et al. (2022a) and Xing et al. (2022). A 50-year return period extreme current above 1.6 m/s is introduced in this paper. Finally, the positional responses of the SST under extreme current are studied using the latest-developed averaged conditional exceedance rate (ACER) method.

This work adapted the hovering control system proposed and tuned by Ma et al. (2022a). Later, the model was extended to investigate the SST depth excursion during aft thruster failure (Xing et al. 2022), which found that response at the SST aft, where thruster failure happens, has a 1.3–2.6 times larger response than the SST bow. This paper will focus on the integrated SST model but consider a 1.6 m/s extreme current speed and more considerable fluctuation. Twenty simulated 4-hour extreme values are used to predict the maximum response of the SST during hovering in extreme currents based on the ACER method. The ACER method, which was proposed in Naess and Gaidai (2009), is a Monte Carlo-based state-of-the-art extreme value prediction method. It has been applied widely in engineering, especially naval architectures, to estimate structural responses (Gaidai et al. 2016; Xu et al. 2019) and sea states, such as wind (Gaidai et al. 2019) and current profiles (Yu et al. 2020). This method is also advanced to solve complex engineering problems with a reduced requirement for the size of data (Gaidai et al. 2022).

The paper structure is organised in the following manner: Section 2 introduces the SST planar model developed in Simulink. The control system is presented in Section 3. Then, Section 4 briefs the mathematics behind the ACER method. After that, the results
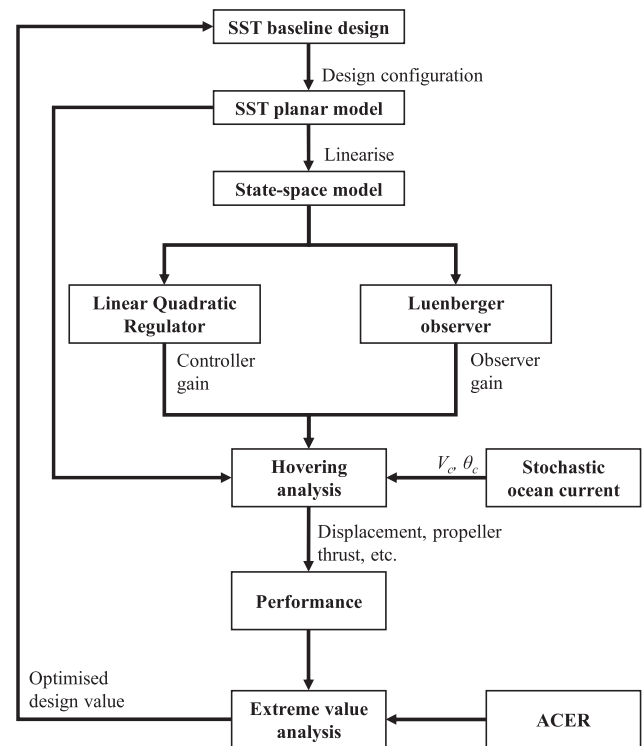
Figure 4. Flowchart describing how hovering analysis under extreme stochastic current is done and how it serves for SST design. (This figure is available in colour online.)

are presented and discussed in Section 5. Finally, the main findings are summarised in Section 6.

2. SST planar model

2.1. Baseline SST design configurations

The most critical design parameters of the baseline SST (Ma et al. 2021) related to offloading modelling and analysis are summarised in Table 1. The coordinate system described in Section 2.2 is used in the table.

The SST hovering system consists of its main propeller, two tunnel thrusters located at the bow and aft, and two compensation tanks situated at the bow and aft compartments for station keeping. The propeller and thrusters ensure that the SST maintains its position facing the current. The compensation tanks compensate for the mass difference sustained during offloading and guarantee the neutral buoyancy of the SST.

Table 1. Subsea shuttle tanker design parameters.

Design configuration	Value	Design configuration	Value
Perpendicular length L_{pp} [m]	164	Bow, aft thruster thrust coefficient K_{Tt} [-]	0.4
Mid-body diameter D [m]	17	Propeller diameter d_p [m]	7
SST mass displacement Δ [tonnes]	33,600	Propeller thrust coefficient K_{Tp} [-]	0.19
Carbon dioxide capacity [m³]	16,362	Safety depth [m]	40
Moment of inertia (pitch) I_{yy} [kg·m²]	3.63×10^9	Nominal diving depth [m]	70
Centre of buoyancy [m]	[0, 0, −0.41]	Collapse diving depth [m]	190
Bow thruster location along SST length x_{tb} [m]	60	Designed collapse pressure [bar]	19
Aft thruster location along SST length x_{ta} [m]	−60	Structural design safety factor	2.7
Bow, aft thruster diameter d_t [m]	2		

2.2. Coordinate system

The longitudinal motion and lateral motion of slender submersibles like submarines and torpedoes are non-interacting (Tinker 1982; Ross et al. 2004). Therefore, it can be divided into longitudinal and lateral subsystems. The longitudinal subsystem is sufficient in this study.

The coordinate system setup of the SST is shown in Figure 5. The body-fixed coordinate system is situated at the subsea shuttle tanker's centre of gravity (CoG). The origin of the SST body frame is relative to a global earth-fixed coordinate system based on the North-East-Down (NED) system. The centre of buoyancy, which is at the centroid of the subsea shuttle tanker, is located slightly above the CoG. In the figure, the positive global surge motion x points to the bow direction and, positive heave motion z points downward, positive pitch motion θ points from z-axis to x-axis; the velocities definition in the body frame are u, w, and q, respectively; the accelerations are $\dot{u}$, $\dot{w}$, and $\dot{q}$ correspondingly.
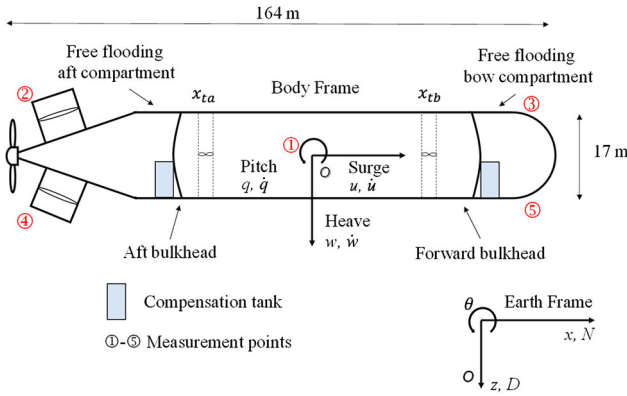

Figure 5. SST body frame and earth frame coordinate system with measurement points. (This figure is available in colour online.)

2.3. Simulink model implementation

As presented in Figure 6, the SST manoeuvring model is broken down into three categories:

- **SST plant model:** the SST plant model considers the hydrodynamic forces contributed by added mass, hydrodynamic drag, and body lift. The mathematic formulation of the plant model is explained in Section 2.4;

- **Actuator model:** the actuation system of the SST consists of the main propeller, tunnel thrusters, compensation (ballast) tanks, and aft hydroplanes. The main propeller, thrusters, and compensation tanks are used during offloading, and they are presented in Sections 2.5 and 2.6.
- **Ocean current model:** the current velocity and direction are modelled as stochastic processes. It is described in Section 2.7.

2.4. Vessel model

The equations of motion of the SST consist of kinetic equations of motion and dynamic equations of motion. Written in vectorial form, they are expressed as:

$$\dot{\eta} = J_\Theta(\eta)v$$
$$M\dot{v} + C(v)v + D(v)v + g(\eta) = \tau \tag{1}$$

In the equations, η is SST motion in global coordinate; v represents the velocity vector; $J_\Theta(\eta)$ is the matrix of Euler transformation; M is the matrix containing the mass and added mass of the SST; $C(v)$ is a matrix containing the Coriolis-centripetal forces; $D(v)$ is a matrix consisting of the hydrodynamic drag forces; $g(\eta)$ is the vector for gravitational and hydrostatic forces; τ is the control force vector.

The first equation can be expanded as:

$$\underbrace{\begin{bmatrix} \dot{N} \\ \dot{D} \\ \dot{\theta} \end{bmatrix}}_{\dot{\eta}} = \underbrace{\begin{bmatrix} \cos\theta & \sin\theta & 0 \\ -\sin\theta & \cos\theta & 0 \\ 0 & 0 & 1 \end{bmatrix}}_{J_\Theta(\eta)} \underbrace{\begin{bmatrix} u \\ w \\ q \end{bmatrix}}_{v} \tag{2}$$

where the notations of the motions are illustrated in Figure 5.

The matrices in the dynamic equations of motion (1) can be expanded as (3)-(5):

$$M = \begin{bmatrix} m - X_{\dot{u}} & 0 & mz_g \\ 0 & m - Z_{\dot{w}} & -Z_{\dot{q}} \\ mz_g & M_{\dot{w}} & I_{yy} - M_{\dot{q}} \end{bmatrix} \tag{3}$$

$$C(v) = \begin{bmatrix} 0 & 0 & 0 \\ 0 & m - Z_{\dot{w}} & -(m - X_{\dot{u}})u \\ 0 & (Z_{\dot{w}} - X_{\dot{u}}) & 0 \end{bmatrix} \tag{4}$$

$$D(v) = \begin{bmatrix} X_{|u|u}|u| & X_{wq}q & X_{qq}q \\ Z_{uq}q & Z_{|w|w} + Z_{uw}u & Z_{q|q|} \\ M_{uw}w & M_{|w|w} & M_{uq}u + M_{|q|q} \end{bmatrix} \tag{5}$$
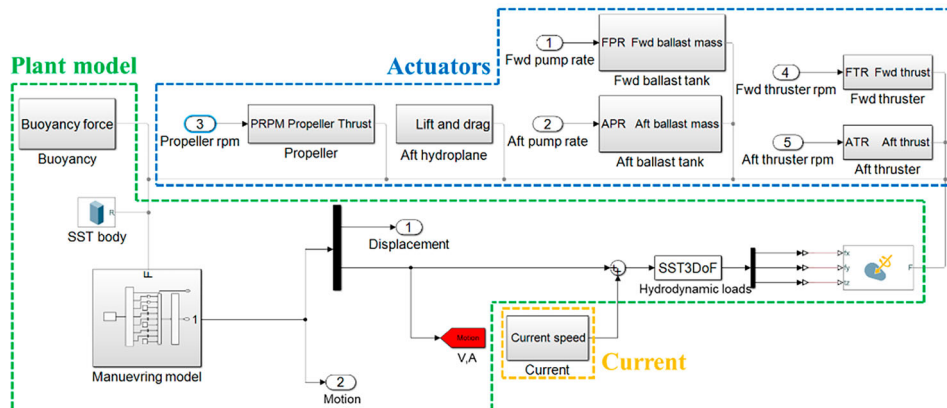

Figure 6. Subsea shuttle tanker manoeuvring model in Simulink. (This figure is available in colour online.)

Table 2. Hydrodynamic derivatives.

Parameter	Value	Unit	Parameter	Value	Unit
$X_{\dot{u}}$	-5.14×10^5	kg	$Z_{|q|q}$	4.79×10^9	kg·m
$Z_{\dot{w}}$	-3.29×10^7	kg	$M_{|q|q}$	-4.34×10^{12}	kg·m²
$M_{\dot{w}}$	-4.40×10^8	kg·m	X_{wq}	-3.28×10^7	kg
$Z_{\dot{q}}$	-4.40×10^8	kg·m	X_{qq}	-4.40×10^8	kg·m
$M_{\dot{q}}$	-6.39×10^{10}	kg·m²	Z_{uq}	5.14×10^5	kg
$X_{|u|u}$	-1.64×10^4	kg/m	M_{uq}	-4.40×10^8	kg·m
$Z_{|w|w}$	-1.42×10^6	kg/m	Z_{uw}	-2.42×10^5	kg/m
$M_{|w|w}$	1.67×10^7	kg	M_{uw}	-3.99×10^7	kg

where $X_{\dot{u}}$, $Z_{\dot{w}}$, $Z_{\dot{q}}$, $M_{\dot{w}}$, and $M_{\dot{q}}$ are added mass hydrodynamic coefficients; $X_{|u|u}$, $Z_{|w|w}$, $Z_{|q|q}$, $M_{|w|w}$, and $M_{|q|q}$ are drag terms; X_{wq}, X_{qq}, Z_{uw}, Z_{uq}, and M_{uq} are cross-term added mass hydrodynamic coefficients; Z_{uw} is the body lift and M_{uw} is the Munk moment. The hydrodynamic derivatives used in this study are listed in Table 2.

2.5. Propeller model

The SST propeller design is provided by Ma et al. (2021), in which a Wageningen B3-30 propeller is selected. It is 3-bladed and has a small aspect ratio of 0.30. The diameter of the propeller d_p is 7 m. During the 4-hour unloading simulation process, the mean current velocity is constant. Consequently, a constant thrust coefficient $K_{Tp} = 0.17$ is used. Therefore, the thrust of the main propeller can be obtained as:

$$F_P = K_{Tp} \cdot \rho \cdot n_p \cdot |n_p| \cdot d_p^4 \tag{6}$$

where ρ is seawater density and n_p is propeller rotational speed.

2.6. Tunnel thruster model

Two identical tunnel thrusters are equipped on the SST for hovering control (Xing et al. 2022; Ma et al. 2022a). Their positions are illustrated in Figure 5 and the configurations are listed in Table 1. The thrusters' forces result in heave forces and pitching moments on the SST. The contribution from individual thruster can be expressed as:

$$F_T = K_{Tt} \cdot \rho \cdot n_t \cdot |n_t| \cdot d_t^4 \tag{7}$$

where F_T is the thruster thrust and n_t is the thruster revolution speed. As the advanced speed for tunnel thrusters is minimal, the advanced number is approximately 0. Consequently, the thruster thrust coefficient is a constant of 0.4.

The thruster vector $\boldsymbol{\tau_T}$ consisting of the propeller and thrusters' contributions in the surge, heave, and pitch can be summarised as:

$$\boldsymbol{\tau_T} = \begin{bmatrix} F_P \\ F_{Tb} + F_{Ta} \\ F_{Tb}x_{Tb} + F_{Ta}x_{Ta} \end{bmatrix} \tag{8}$$

where F_{Tb} and F_{Ta}, as calculated by (7), are thrusts from the bow and aft thrusters, respectively.

2.7. Stochastic current model

Numerous research and guidelines have introduced the modelling of stationary current (DNV 2010; Yu et al. 2020; Domps et al. 2021). However, these models are not sufficient to study the positioning problem of the SST subjected to time-varying current. Therefore, a stochastic current model presented by Fossen (2021) and Sørensen (2018) is adapted to this study to consider current velocity variation. The current is represented by two variants: current

velocity V_c and current inflow angle θ_c. They both follow the first-order Gauss-Markov process:

$$\dot{V}_c + \mu_1 V_c = \omega_1 \tag{9}$$

$$\dot{\theta}_c + \mu_2 \theta_c = \omega_2 \tag{10}$$

where μ_1 and μ_2 are time constants with nonnegative values, according to Fossen (2021). ω_1 and ω_2 are Gaussian white noise. To exemplify, the time constants are set to be 1 in this work. The noise power of the Gaussian white noise is set to 0.1 when rendering the turbulency of the inflow.

For 2D irrotational current, the current velocity in the global frame can be expressed as:

$$\boldsymbol{v_c^g} = \begin{bmatrix} V_c \cos\theta_c \\ V_c \sin\theta_c \\ 0 \end{bmatrix} \tag{11}$$

Therefore, the current velocity described in the SST body frame can be expressed as:

$$\boldsymbol{v_c^b} = \begin{bmatrix} V_c \cos(\theta_c - \theta) \\ -V_c \sin(\theta_c - \theta) \\ 0 \end{bmatrix} \tag{12}$$

Finally, the relative velocity is obtained by summing up $\boldsymbol{v_c^b}$ and $\dot{\boldsymbol{\eta}}$.

Current data in the North Sea is used as the baseline SST designed to be deployed in the Norwegian sector. Extreme current velocity is determined based on the work conducted in Pugh (1982), which estimated the extreme current distributions and velocities by applying joint tide-surge probability techniques to the observation data in Inner Dowsing, North Sea. The extreme current prediction result is summarised in Figure 7. The figure shows that the maximum current velocity is observed at the South-West 165 ° direction, where the corresponding extreme current speed is 1.6 m/s with a 50-year return period. This value is then used as the mean current velocity to generate the stochastic current time domain realisation.
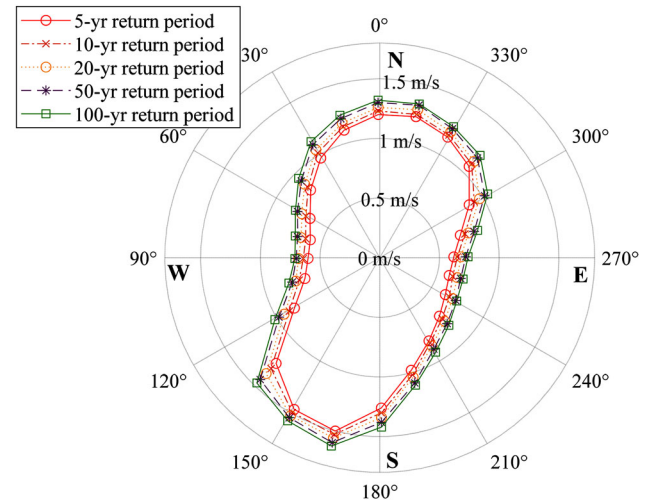
Figure 7. Extreme current velocity distribution at Inner Dowsing (data from Pugh (1982)). (This figure is available in colour online.)

3. Control system design

The control system used for the SST hovering, an LQR, was initially designed by Ma et al. (2022a) and then extended by Xing et al. (2022). The control diagram is presented in Figure 8. An LQR is
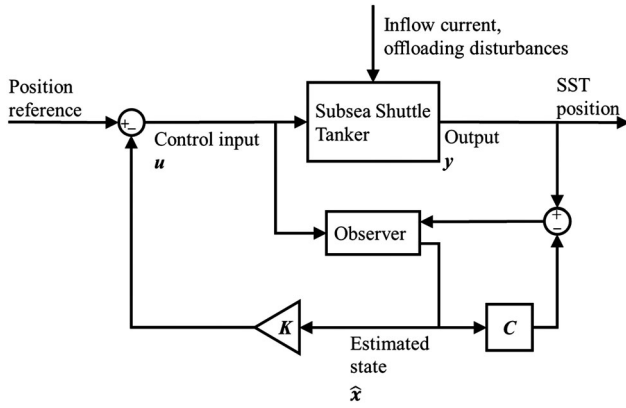
Figure 8. SST control block diagram. (This figure is available in colour online.)

a full-state feedback optimal control method which aims to solve the optimisation problem at hand, i.e. performance versus effort, and thereby find the state feedback controller gain K. Defining the performance and effort parameters will be influenced by the desired properties of the subsea shuttle tanker. E.g. one specific gain matrix can be determined by imposing importance on the stability of the subsea shuttle tanker under the offloading process (i.e. a minimal movement is required). This would increase actuator efforts and consequently reduce the energy storage and subsea shuttle tanker range at a higher rate.

$$A = \begin{bmatrix} 0 & 0 & 0 & 1 & 0 & 0 \\ 0 & 0 & 0 & 0 & 1 & 0 \\ 0 & 0 & 0 & 0 & 0 & 1 \\ 0 & 0 & 2.65 \times 10^{-5} & -1.00 \times 10^{-3} & -1.21 \times 10^{-4} & -1.45 \times 10^{-2} \\ 0 & 0 & 2.87 \times 10^{-6} & -1.32 \times 10^{-4} & -8.91 \times 10^{-3} & 5.18 \times 10^{-2} \\ 0 & 0 & -2.37 \times 10^{-2} & 6.21 \times 10^{-5} & 3.87 \times 10^{-3} & -5.96 \times 10^{-2} \end{bmatrix} \tag{15}$$

On the other hand, if the design of the subsea shuttle tanker would present more flexibility in the movement during offloading, we would penalise actuator effort to reduce the energy consumption during the offloading process. This would then give us a different gain matrix K.

3.1. Linear state-space model

3.1.1. Linear state-space function
The SST model is highly coupled, non-linear, and time-variant. In the design of an LQR, a linear time-invariant state-space model is obtained using a MATLAB model linearizer. The linear state-space equations for the subsea shuttle tanker are presented in (13) and (14):

$$\dot{x} = Ax + Bu \tag{13}$$

$$y = Cx \tag{14}$$

where x represents the state of the system (state vector), and y represents the output of the system (output vector). The vector u is called the control vector and represents the control input. Matrix A, B and C are state, input, and output matrices, respectively.

3.1.2. Model linearisation
The subsea shuttle tanker manoeuvring is dynamic, non-linear, and coupled by nature. By linearising the model, we can attain the linear space-state function.

- Input of linearised model, $u = [n_{tb}; n_p; n_{ta}]$;
- Output of linearised model, $y = [N; D; \theta]$;
- Obtained state vector, $x = [N; D; \theta; \dot{N}; \dot{D}; \dot{\theta}]$.

The linearisation approximation of the non-linear system will only be valid in a small region around the chosen operating point. The relevant operating point for the linearisation of the manoeuvring model is specified as a 1 m/s design current speed with an inflow angle of 1 °. A, B and C are a 6×6, 6×3, and 3×6 matrices, respectively. The linearised state-space model is obtained as follows:

$$B = \begin{bmatrix} 0 & 0 & 0 \\ 0 & 0 & 0 \\ 0 & 0 & 0 \\ 2.54 \times 10^{-10} & -8.80 \times 10^{-5} & 4.24 \times 10^{-10} \\ 3.84 \times 10^{-6} & -5.25 \times 10^{-9} & 6.40 \times 10^{-6} \\ 7.13 \times 10^{-7} & 0 & -1.19 \times 10^{-6} \end{bmatrix} \tag{16}$$

$$C = \begin{bmatrix} 1 & 0 & 0 & 0 & 0 & 0 \\ 0 & 1 & 0 & 0 & 0 & 0 \\ 0 & 0 & 1 & 0 & 0 & 0 \end{bmatrix} \tag{17}$$

3.2. Linear quadratic regulator

As the LQR is an optimal control, it aims to solve the optimisation problem, i.e. performance versus effort, and thereby find the gain matrix K. For the time-invariant system expressed in (13) and (14), the LQR solves the quadratic weighted cost functions and approaches the optimal gain based on our weighted performance and effort (Fossen 2021).

Equation (29) shows the minimised quadratic cost function, where Q represents the performance and R represents the effort.

$$L(x, u) = \int_0^\infty (x^T Q x + u^T R u) dt \tag{18}$$

The state weighting matrix is defined as $Q = Q^T \geq 0$, and the energy weighting matrix for the actuator is defined as $R = R^T \geq 0$. These weighting matrices give us the importance of the state error together with the power consumption of the actuator system.

By differentiating between the initial state of the system and the desired state of the system, we can penalise the different states and efforts, i.e. adjusting the diagonal elements in the matrix Q and R, respectively. By doing this, the most optimal solution based on our relative weights of the performance and effort is obtained.

The control law for LQR is obtained by solving the LQR problem and is described as:

$$u = -Kx \tag{19}$$

where the gain matrix K is a 3×6 matrix derived from an optimisation problem.

When designing a linear quadratic regulator, the controllability of the subsea shuttle tanker must be satisfied. The linear state matrix A and linear input matrix B must be controllable for the planar

model. The controllability matrix **Con** must have full rank (i.e. its rank, number of linearly independent rows equals the largest possible for the matrices of the same dimensions) and must thus have a right inverse.

$$Con = [B|AB|\dots|A^{n-1}B] \tag{20}$$

The controllability matrix for the subsea shuttle tanker linearised model displays a controllability matrix of 6, i.e. the system is controllable.

3.3. State observer

As Figure 8 displays, a Luenberger observer (state observer or state estimator) (Luenberger 1971) is included in the block design for monitoring the system states. By representing sensors, the Luenberger observer is a system that estimates the internal state of the subsea shuttle tanker. Understanding the internal states of the physical subsea shuttle tanker system during offloading is critical for the design of the motion controller. The estimated state $\hat{x}$ is based on the control input u and the system output y. The system is assumed to be observable, and the system's state can thus be constructed by u and y in a finite time interval.

The observer is mathematically modelled as per (21).

$$\dot{\hat{x}} = Ax + Bu + K_L(y - \hat{y}) \tag{21}$$

where K_L represents the observer gain and $\hat{y}$ is an estimation of the output vector y. Ma et al. (2022a) performed the observer gain sensitivity analysis, which shows that the observer performance increases with moving the pole position further to the negative axis. Identical to Ma et al. (2022a), the pole position of $p = [-4; -4; -4; -2; -2; -2]$ is used in this work.

Similarly, the system needs to be observable before implementing the Luenberger observer; the observability matrix **Obs** (22) of the SST has a full column 6.

$$Obs = [C^\top|A^\top C^\top|\cdots|(A^\top)^{n-1}C^\top] \tag{22}$$

4. Average conditional exceedance rate method

The average conditional exceedance rate (ACER) is used in extreme value predictions and distributions, and the method was introduced by Naess and Gaidai (2009). This extreme value prediction is made by constructing a series of non-parametric functions not based on asymptotic sample theory. The method has been applied for stationary and non-stationary stochastic processes and includes all global maximum peaks. It also avoids the necessity of declustering of data to ensure independence (Karpa 2015). From Xing et al. (2022), it was manifested that the extreme responses were twice as high for a 5-year return period compared to the maxima of a 4-hour response period.

Naess and Moan (2013) claims that for response processes of marine structures, the Gumbel distribution would almost always be the appropriate one. However, Gumbel distribution does not have an upper limit in its prediction, unlike most engineering problems. This makes the Gumbel distribution tends to be over-conservative and overpredicts the extreme value. Xing et al. (2022) compared the ACER method with Gumbel when studying the SST hovering problem under low current speed subjected to aft thruster failure. It verified the robustness of the ACER method used in novel concepts. It also found that the ACER method can better estimate the exact extreme value without involving asymptotic assumptions. Compared to other extreme value estimation techniques such as generalised extreme value distribution and peaks-

over-threshold method, ACER does not require the observations to be independent and identically distributed, i.e. each random variable will have the same probability distribution as the other random variables. No outcome will influence other outcomes (independent), and all samples come from the same distribution (identical). The non-parametric functions based on ACER functions of various orders are developed, and the aim is to approximate the actual extreme value distribution.

In detail, the ACER method determines the distribution function of the extreme value, which is denoted $M_N = max\{X_j; j = 1, \cdots, N\}$. An accurate estimation of $P_\eta = Prob(M_N \leq \eta)$ is wanted for large values of η. It denotes the probability of the occurrence of the extreme value η and it follows:

$$P_\eta = Prob(M_N \leq \eta) = Prob(X_1 \leq \eta, \cdots, X_N \leq \eta) \tag{23}$$

Solving this equation, a succession of conditional approximation $P_k(\eta)$ is used, where $P_k(\eta)$ tends to be close to P_η as k increases. For $N \gg 1$ and $k = 1, 2, \cdots, P_k(\eta)$ is represented as (Naess and Gaidai 2009):

$$P_k(\eta) \approx exp\left(-\sum_{j=k}^{N} \alpha_{kj}(\eta)\right) \tag{24}$$

where $\alpha_{kj}(\eta) = Prob(X_1 > \eta|X_{j-1} \ll \eta, \cdots, X_{j-k+1} \leq \eta)$ and it represents the exceedance probability (only counted if proceeded by non-exceedances). The notion described in (24) and will be calculated by ACER as follows:

$$\varepsilon_k(\eta) = \frac{1}{N-k+1}\sum_{j=k}^{N} \alpha_{kj}(\eta), k = 1, 2, \cdots \tag{25}$$

where N represents the number of sample points for a specific moment X_n. Onwards, for $k \geq 2$, $\tilde{\varepsilon}_k(\eta)$ is used instead of $\varepsilon_k(\eta)$. This is done because it is easier to use for non-stationary or long-term statistics (Naess and Moan 2013), and it is defined as:

$$\tilde{\varepsilon}_k(\eta) = \lim_{N \to \infty} \frac{\sum_{j=k}^{N} a_{kj}(\eta)}{N-k+1} \tag{26}$$

$$\lim_{N \to \infty} \frac{\tilde{\varepsilon}_k(\eta)}{\varepsilon_k(\eta)} = 1. \tag{27}$$

where $a_{kj}(\eta)$ is the realised values for the observed time series, and (27) needs to be fulfilled. The ACER (for both stationary and non-stationary time series) sample estimate can be denoted as:

$$\hat{\varepsilon}_k(\eta) = \frac{1}{R}\sum_{r=1}^{R} \hat{\varepsilon}_k^{(r)}(\eta) \tag{28}$$

where R is the number of samples or realisations, and

$$\hat{\varepsilon}_k^{(r)}(\eta) = \frac{\sum_{j=k}^{N} a_{kj}^{(r)}(\eta)}{N-k+1} \tag{29}$$

where r denotes the specific realisation number.

With sufficient numbers of realisations and assumed independent, the 95% confidence interval (CI) for the $\varepsilon_k(\eta)$ can be estimated as:

$$CI(\eta) = \hat{\varepsilon}_k(\eta) \pm \frac{1.96\hat{s}_k(\eta)}{\sqrt{R}} \tag{30}$$

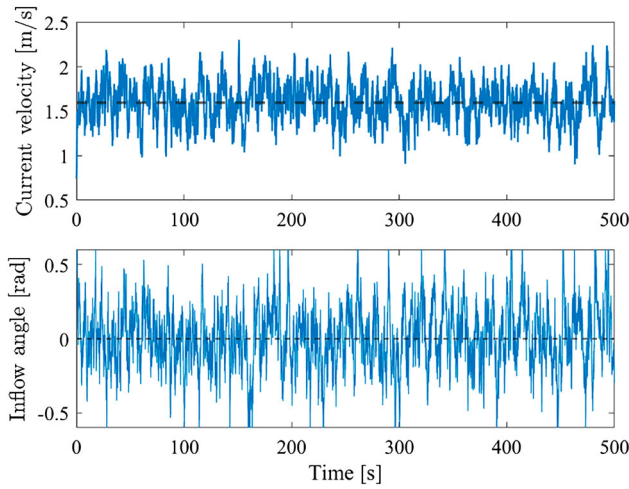where $\hat{s}_k(\eta)$ refers to the sample standard deviation of samples and

Figure 9. Exemplified current realisation. (This figure is available in colour online.)

can be estimated by:

$$\hat{s}_k(\eta)^2 = \frac{1}{R-1} \sum_{r=1}^{R} (\hat{\varepsilon}_k^{(r)}(\eta) - \hat{\varepsilon}_k(\eta))^2 \tag{31}$$

The above equations for estimation of average exceedance rate are based on direct numerical simulations. In contrast, an extrapolation technique can reduce the computational time. Assuming the mean exceedance rate in the tail behaves similarly to $exp\{-a(\eta - b)^c\}$ ($\eta \geq \eta_0 \geq b$) where a, b and c are suitable constants. The ACER will therefore be assumed by:

$$\varepsilon_k(\eta) \approx q_k(\eta)exp\{-a_k(\eta - b_k)^{c_k}\} \tag{32}$$

where $\eta \geq \eta_1 \geq b_k$ and the function $q_k(\eta)$ varies slowly compared to the exponential function $exp\{-a_k(\eta - b_k)^{c_k}\}$ in the tail region. Continuously, this can be replaced by a constant for a fitting choice of the tail marker η_0. In the end, the Levenberg-Marquardt least-squares optimisation method can be used to determine the constants a_k, b_k, c_k and q_k. Naess and Gaidai (2009) expressed their experience that this damped least-squares method is well suited for this assignment. Chai et al. (2018) concluded that the extrapolation scheme applied to capture the tail behaviour of the ACER functions was satisfactory for the extreme value predictions.

5. Results and discussion

5.1. Time-domain response

In total, an 80-hour realisation consisting of 20 independent 4-hour simulations is performed in Simulink. Figure 9 exemplifies a 500 s stochastic current realisation. The mean current velocity is set to be 1.6 m/s while the mean inflow angle is 0 °. Correspondingly, Figure 10 exemplifies the response of the SST, i.e. SST state vector $x = [N; D; \theta; \dot{N}; \dot{D}; \dot{\theta}]$, in the global coordinate system to present the performance of the controller and the observer. Both measured states and actual states are given. As shown in Figure 10 (a), the observer can provide excellent measurement for the SST surge, heave, and pitch displacement, as shown in Figure 10 (b), the observed values for surge, heave, and pitch velocities are close to the actual velocities of the SST. In the presented time series, the SST has a steady surge off-site of approximately 1.2 m with a fluctuation amplitude of about 0.2 m. On the contrary, the heave motion of the SST has an amplitude of around 2 metres, significantly more significant than the surge displacement. This is caused by the giant side-way drag force. The pitch motion of the SST in the presented case is lower than 0.04 rad. As the SST has a length of 164 m, this can still result in an over 2 metres off-site to the bow and aft. Figure 11 (a) and (b) present the power spectral density (PSD) of the heave and pitch motions, respectively. It can be observed that the peak of heave motion is at a frequency approximately 5×10^{-4} Hz, equivalently at the eigen period of about 30 min. The peak of pitch motion is at a frequency approximately 0.017 Hz, equivalently at the eigen period of about 10 min.

From the SST time series, the responses of the five measurement points (ref. Figure 5) are obtained. The maximum and minimum depth excursions in the 20 realisations for the five points are presented in Figure 12 (a) and Figure 12 (b). These are the inherent values to study the depth excursions of the SST and further predict the long-term extreme depth off-site of the SST, which helps determine the values bringing a cost-efficient design. Essentially, the extreme depth excursions happen at the vessel's bow and aft, rather than the positions close to the mid-vessel, as the motions at those positions have contributed from the pitch motion. Therefore, the minimum depth excursions are expected at the bow and aft of the upper bound of the SST, i.e. Point 3 and Point 2, as shown in Figure 12 (b). While the maximum depth is reached by the bow and aft of the lower bound, i.e. Point 4 and Point 5, measurement point 1 locates at the centroid of the SST and is provided as a reference.
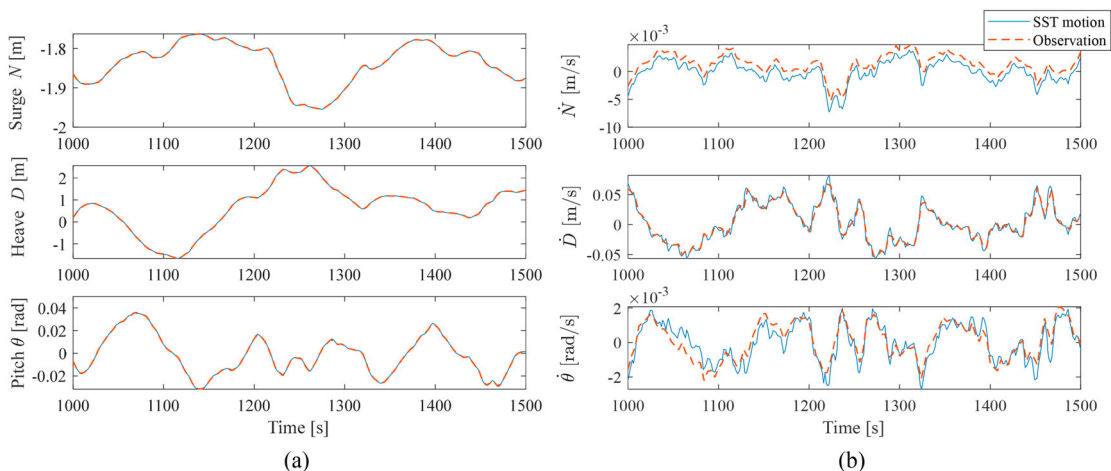

Figure 10. SST response in 500 s realisation. (a) SST motion. (b) SST velocity. (This figure is available in colour online.)
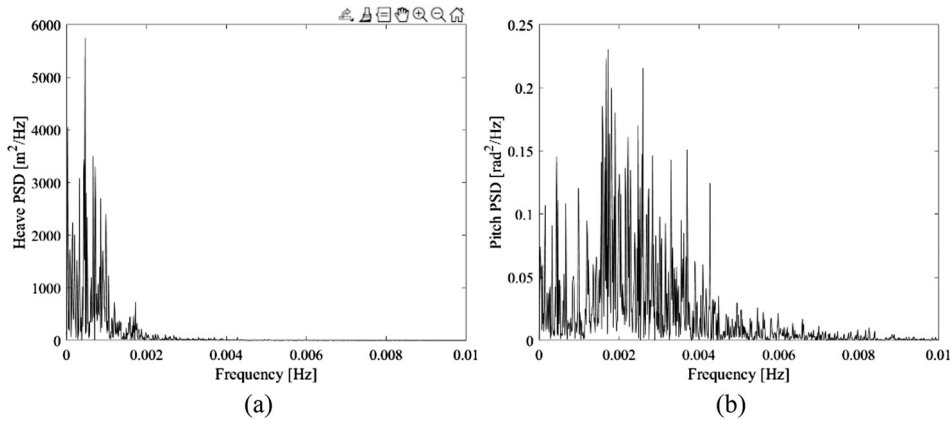
Figure 11. Power spectral density for the (a) heave and (b) pitch of the SST. (This figure is available in colour online.)
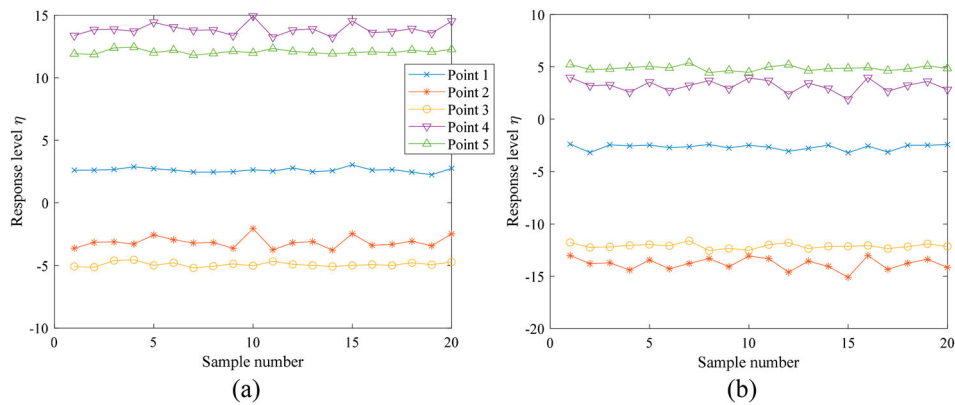

Figure 12. Maximum and minimum depth off-site for the points of interest in each realisation. Point 1–5 are illustrated in Figure 5. (a) Maximum depth excursion. (b) Minimum depth excursion. (This figure is available in colour online.)
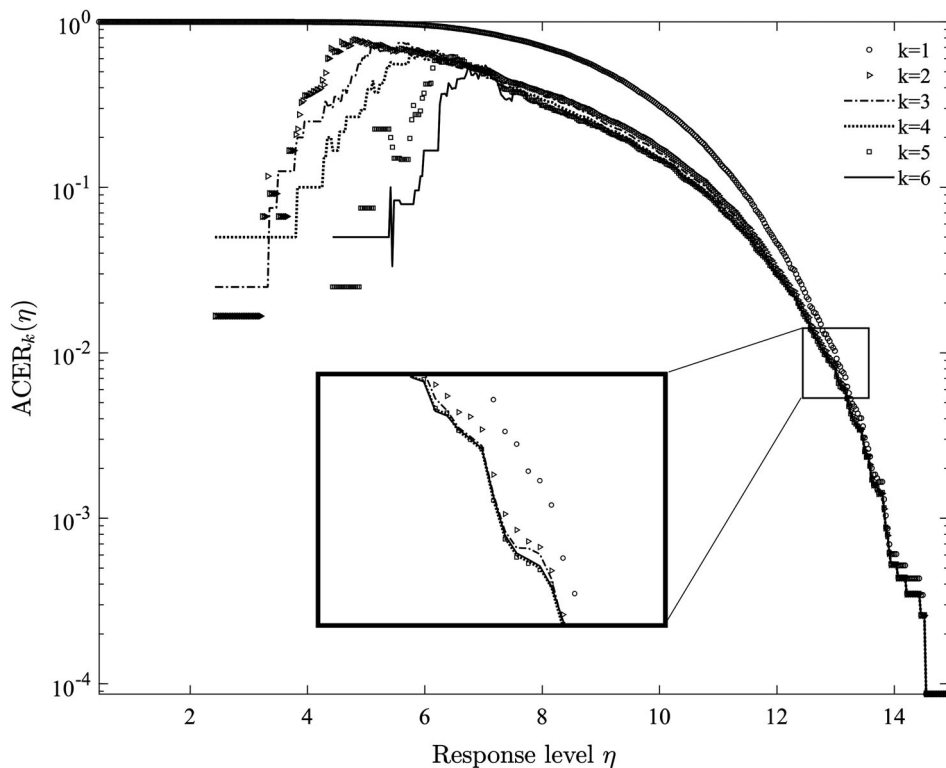

Figure 13. ACER functions for maximum depth excursion of Point 4 with different *k* values. (This figure is available in colour online.)
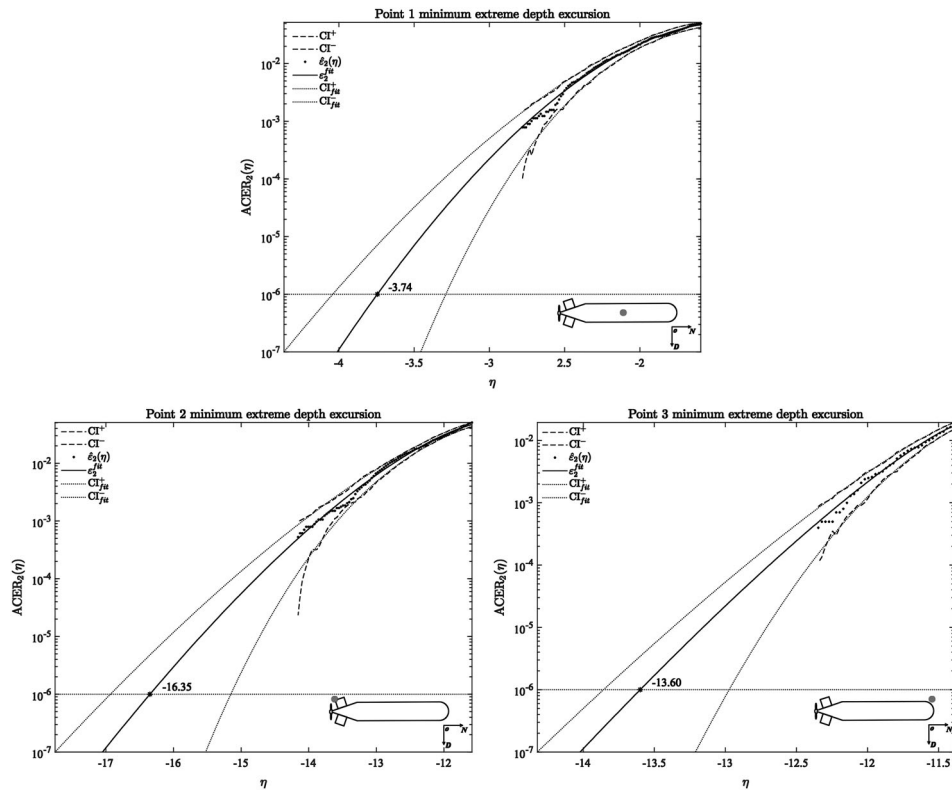
Figure 14. ACER extrapolation for minimum depth excursion. (a) Point 1. (b) Point 2. (c) Point 3. (This figure is available in colour online.)
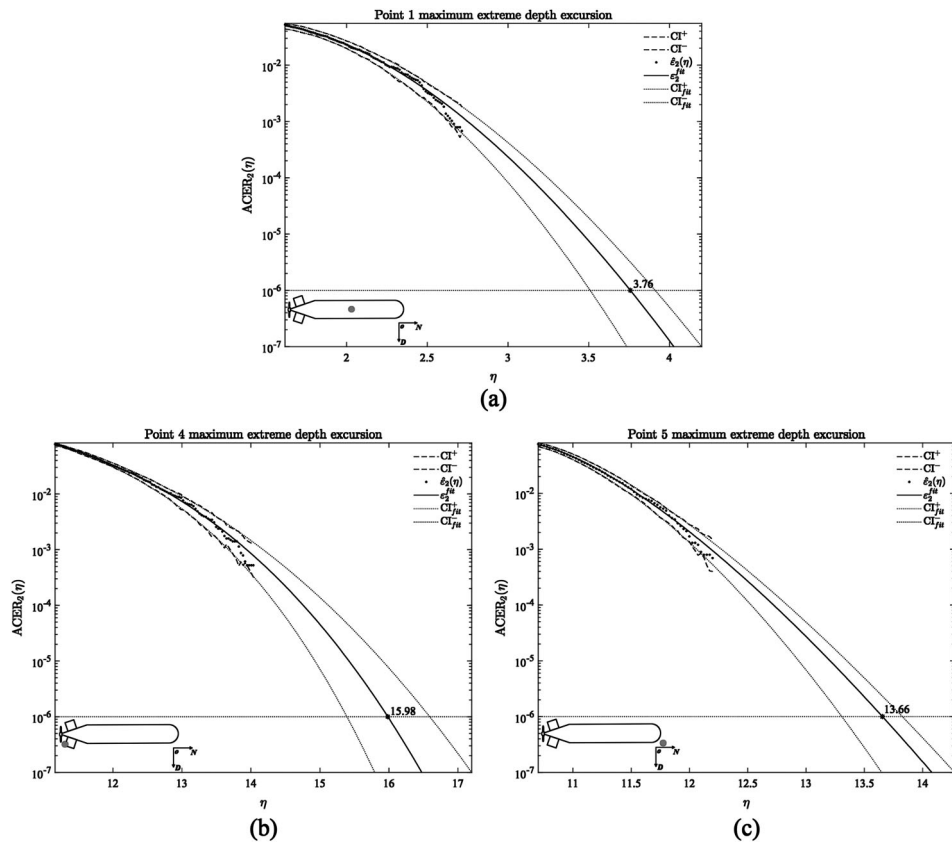

Figure 15. ACER extrapolation for maximum depth excursion. (a) Point 1. (b) Point 4. (c) Point 5. (This figure is available in colour online.)

Table 3. Extreme value responses using ACER method for an exceedance rate of 1×10^{-6}; 95% CI in paratheses.

Extreme depth	Measurement point	Extrapolation value	95% CI⁻	95% CI⁺
Minimum depth	Point 1	−3.74431	−3.28976	−4.04082
	Point 2	−16.3476	−15.1519	−16.9326
	Point 3	−13.5987	−12.9733	−13.8570
Maximum depth	Point 1	3.75786	3.50877	3.91145
	Point 4	15.9833	15.3909	16.5901
	Point 5	13.6554	13.3068	13.8259

Table 4. SST depth excursion response predictions with 1-year and 5-year return period.

Point number	Exceedance rate	Equivalent return period	Extrapolation value
Point 2	3.7×10^{-5}	1-year	−15.1
	7.6×10^{-6}	5-year	−15.7
Point 4	3.7×10^{-5}	1-year	15.0
	7.6×10^{-6}	5-year	15.5

5.2. *k* value selection

As mentioned in Section 4 and Naess and Gaidai (2009), the cascade of conditioning approximations $P_k(\eta)$ converge toward $P(\eta)$ when k increases. k value from 1–6 is checked in this study. The result for Point 4 maximum depth excursion is presented, for instance, in Figure 13. It can be noticed that for k from 1 to 6; the response η is at the same level. However, with the same $ACER_k(\eta)$, η is more conservative (larger) for $k = 1$ while the values for $k \geq 2$ are very close. Therefore, it is concluded that applying $k = 2$ returns an accurate prediction of the SST extreme depth excursion for the measured points.

5.3. Extreme depth excursion predicted by ACER method

The extreme depth excursions of the SST measurement points using the ACER method for the 80-hour simulations are discussed in this section. Figure 14 and Figure 15 present the extrapolation results with an exceedance rate of 1×10^{-6} of the minimum and maximum depth excursion, respectively. This is close to a 50-year return period. The 95% confidence interval (CI) is presented in a dashed line, and the fitted 95% CI is presented in dotted lines. A close fit to the simulation results can be observed for the ACER method.

The minimum extreme response of the SST is observed at Point 2, as shown in Figure 14 (b). The value with a 1×10^{-6} exceedance rate is −16.35 m from the reference offloading position, 2.75 m

above the value for the SST bow. As a reference, this extreme value for the SST centroid (Point 1) is −3.74 m. The results indicate that if the SST offloads at 40 m safety depth, the minimum extreme depth excursion is 23.65 m (upper bound).

The maximum positive off-site (lower bound) is also observed at the aft (Point 4). Its value is 15.98 m, slightly lower than the absolute minimum depth excursion (16.35 m). The maximum extreme depth at the SST bow (Point 5) is 2.32 m smaller. The maximum extreme off-site for Point 1 is 3.74 m, the same as the absolute minimum extreme. Therefore, when the SST is offloading at a 70 m water depth, the maximum depth excursion of the SST with a 1×10^{-6} exceedance rate is 86 m.

Finally, the ACER prediction results are summarised in Table 3. The extrapolation result of 1-year motion and 5-year motion for points 1 and 4 are presented in Table 4. The main findings in this paper are denoted in Figure 16. The SST's permissible offloading depth region is between 40 m safety depth and 70 m nominal diving depth. However, under a 1.6 m/s extreme current condition, the maximum depth excursion can reach 86 m while the minimum extreme depth is 23.65 m. From the design perspective, it can be noticed that the maximum depth excursion is far from the 190 m collapse diving depth. This indicates that the guidelines are over-conservative in terms of defining the collapse pressure of the SST. With a better understanding of the SST, this value can be largely reduced. From the operation perspective, the SST should offload at least 16 m above the upper bound of any subsea installations in order to reduce the risk of collision. Also, the maximum draught of any surface/floating installations should be smaller than 23 m, i.e. the minimum depth excursion when the SST is offloading at the minimum allowable operation depth in the region of SST operation. Similarly, when an SST is offloading in fields with large draught floating structures, a 16 m minimum safety depth distance should always be maintained.

6. Conclusion

A novel autonomous subsea shuttle tanker concept was proposed as a cost-effective method of transporting liquid CO_2 from shore & offshore facilities to subsea wells for enhanced oil recovery or permanent storage. However, the design of such a large autonomous underwater vehicle has not been detailed investigated. The current existing engineering codes tend to be very conservative by requiring a significant safety factor which will further result in a heavy structural design. Therefore, knowing the maximum response of the SST will benefit the study of such merchant underwater vehicles in two
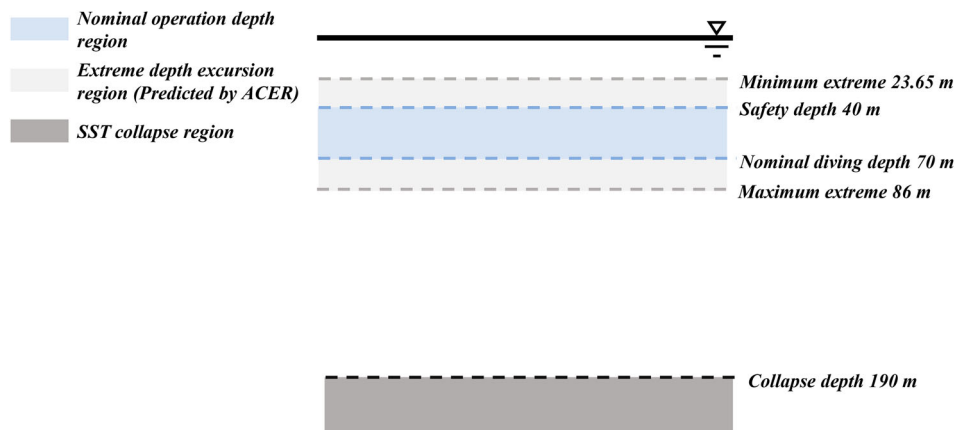
Figure 16. Depth region of SST offloading. (This figure is available in colour online.)

ways: first, knowing the extreme depth excursion unveils the maximum potential off-site of the SST during offloading. This reduces the level of uncertainty and denotes a less conservative design by knocking down the safety factor of the structural design. In addition, the extreme depth excursion can also provide a basis for the decision-makers in terms of SST operation. This study clarifies the maximum and minimum off-site of the SST from its desired offloading reference point. It determines the required minimum safety distance from subsea installations and floating structures during offloading.

This paper studies the extreme response of the SST hovering during offloading. Firstly, a 2D planar model is presented based on the baseline design configurations. The model consists of a rigid SST hull model that considers the hydrodynamic loads acting on the body, the main propeller and two tunnel thrusters located at the front and the aft to keep it stationary under incoming stochastic current. A first-order Gauss-Markov process describes the time-variant stochastic current. The mean current velocity is set to be 1.6 m/s, corresponding to observation data in the North Sea with a return period of 50 years. Later, the SST planar model is streamlined to a linear state-space representation to obtain the controller gain and observer design. During the time-domain simulation, the SST's motion was first measured by the designed Luenberger observer and then passed to the LQR to calculate control inputs. 20 4-hour simulations are performed to get the SST response. Then, the extreme responses with the exceedance rate of 1×10^{-6} from 5 measurement points located at the SST centroid, upper-aft, upper-bow, lower-aft, and lower-bow are studied using the ACER method. The main findings are summarised as follows:

- Effect of k value from 1 to 6 is studied, and the result shows that $k \geq 2$ can provide a very accurate prediction of the SST extreme response during hovering.
- The collapse design of the SST proposed by DNVGL-RU-NAVAL-Pt4Ch1 is very conservative for the SST. The extreme depth excursion happens at the SST aft during hovering, and the maximum depth excursion is 86 m. This means the 19 bar (corresponds to 190 m water depth) collapse pressure can be significantly reduced.
- From an operational perspective, a minimum 16 m safety distance is suggested for the SST hovering. The SST should stay away from any subsea or floating structures with a minimum 16 m distance to avoid a potential collision.
- When the SST is offloading at a 40 m safety depth, the maximum draught of the floating structures in the vicinity should be less than 23 m.

Acknowledgements

Disclosure statement

No potential conflict of interest was reported by the author(s).

ORCID

Yucong Ma http://orcid.org/0000-0002-6225-8184
Yihan Xing http://orcid.org/0000-0003-0883-4854

References

Bai Y, Bai Q. 2018. Subsea engineering handbook. MA, USA and Oxford, UK: Gulf Professional Publishing.

Burcher R, Rydill L. 1994. Concepts in submarine design. Cambridge: Cambridge University Press.

Chai W, Leira BJ, Naess A. 2018. Probabilistic methods for estimation of the extreme value statistics of ship ice loads. Cold Reg Sci Technol. 146:87–97. doi:10.1016/j.coldregions.2017.11.012.

DNV. 2010. DNV-RP-C205 environmental conditions and environmental loads. Oslo, Norway: Det Norske Veritas.

DNV. 2018. Rules for Classification, Naval Vessels, Part 4 Sub-surface Ships, Chapter 1 Submarines. In.

Domps B, Dumas D, Guérin C-A, Marmain J. 2021. High-frequency radar ocean current mapping at rapid scale with autoregressive modeling. IEEE J Oceanic Eng. 46:891–899. doi:10.1109/JOE.2020.3048507.

Ellingsen KE, Ravndal O, Reinås L, Hansen JH, Marra F, Myhre E, Dupuy PM, Sveberg K. 2020. RD 677082-Subsea shuttle system. Res Discl.

Equinor Energy AS. 2019. RD 662093-Subsea shuttle system. Res Discl.

Fossen TI. 2021. Handbook of marine craft hydrodynamics and motion control, Second ed. West Sussex, UK: John Wiley & Sons.

Gaidai O, Fu S, Xing Y. 2022. Novel reliability method for multidimensional nonlinear dynamic systems. Marine Struct. 86:103278. doi:10.1016/j.marstruc.2022.103278.

Gaidai O, Naess A, Karpa O, Cheng Y, Ye R. 2019. Improving extreme wind speed prediction for North Sea offshore oil and gas fields. Appl Ocean Res. 88:63–70. DOI:10.1016/j.apor.2019.04.024.

Gaidai O, Storhaug G, Naess A. 2016. Extreme large cargo ship panel stresses by bivariate ACER method. Ocean Eng. 123:432–439. doi:10.1016/j.oceaneng.2016.06.048.

Karpa O. 2015. Development of bivariate extreme value distributions for applications in marine technology [Doctoral theses]. Trondheim, Norway: Norwegian University of Science and Technology.

Luenberger D. 1971. An introduction to observers. IEEE Trans Autom Control. 16:596–602. doi:10.1109/tac.1971.1099826.

Ma Y, Xing Y. 2022. Identification of the safety operating envelope of a novel subsea shuttle tanker. Ocean Eng. 266:112750. doi:10.1016/j.oceaneng.2022.112750.

Ma Y, Xing Y, Ong MC, Hemmingsen TH. 2021. Baseline design of a subsea shuttle tanker system for liquid carbon dioxide transportation. Ocean Eng. 240. DOI:10.1016/j.oceaneng.2021.109891.

Ma Y, Xing Y, Silva MS, Sui D. 2022a. Modelling of a subsea shuttle tanker hovering in ocean currents. Proceedings of the 41st International Conference of Ocean, Offshore and Arctic Engineering, 2022a June 5–10, Hamburg, Germany.

Ma Y, Xing Y, Sui D. 2022b. Trajectory envelope of a subsea shuttle tanker hovering in stochastic ocean current - model development and tuning. J Offshore Mech Arct Eng. DOI:10.1115/1.4055282.

Naess A, Gaidai O. 2009. Estimation of extreme values from sampled time series. Structural Safety. 31:325–334. DOI:10.1016/j.strusafe.2008.06.021.

Naess A, Moan T. 2013. Stochastic dynamics of marine structures. Cambridge, UK: Cambridge University Press.

Papanikolaou A. 2014. Ship design: methodologies of preliminary design. Dordrecht Heidelberg New York London: Springer.

Patel K, Ma Y, Xing Y, Li L. 2023. Modeling and analysis of the bending moment in a subsea shuttle tanker under the effect of waves using a multi-body approach. Proceedings of the ASME 2023 42nd International Conference on Ocean, Offshore and Arctic Engineering, 2023 June 11–16, 2023, Melbourne, Australia.

Pugh DT. 1982. Estimating extreme currents by combining tidal and surge probabilities. Ocean Eng. 9:361–372. DOI:10.1016/0029-8018(82)90029-4.

Renilson M. 2018. Submarine hydrodynamics, 2 editor. Cham, Switzerland: Springer International Publishing AG.

Ross A, Fossen TI, Johansen TA. 2004. Identification of underwater vehicle hydrodynamic coefficients using free decay tests. Proceedings of the IFAC Conference on Computer Applications in Marine Systems, 2004 7–9 July, Ancona, Italy. doi:10.1016/s1474-6670(17)31759-7.

Sørensen AJ. 2018. Marine cybernetics (lecture notes). Trondheim, Norway: Norwegian University of Science and Technology.

Tinker SJ. 1982. Identification of submarine dynamics from free-model test. Proceedings of the DRG Seminarr on Advanced Hydrodynamic Testing Facilities, 1982, Netherlands.

Xing Y, Gaidai O, Ma Y, Naess A, Wang F. 2022. A novel design approach for estimation of extreme responses of a subsea shuttle tanker hovering in ocean current considering aft thruster failure. Appl Ocean Res. 123:103179. doi:10.1016/j.apor.2022.103179.

Xing Y, Ong MC, Hemmingsen T, Ellingsen KE, Reinås L. 2021a. Design considerations of a subsea shuttle tanker system for liquid carbon dioxide transportation. J Offshore Mech Arct Eng. 143. doi:10.1115/1.4048926.

Xing Y, Santoso TAD, Ma Y. 2021b. Technical–economic feasibility analysis of subsea shuttle tanker. Journal of Marine Science and Engineering. 10:20. doi:10.3390/jmse10010020.

Xu S, Ji C, Soares CG. 2019. Estimation of short-term extreme responses of a semi-submersible moored by two hybrid mooring systems. Ocean Eng. 190:106388. doi:10.1016/j.oceaneng.2019.106388.

Yu S, Wu W, Xie B, Wang S, Naess A. 2020. Extreme value prediction of current profiles in the South China Sea based on EOFs and the ACER method. Appl Ocean Res. 105:102408. doi:10.1016/j.apor.2020.102408.

Zhao X, Liu Y, Han M, Wu D, Li D. 2016. Improving the performance of an AUV hovering system by introducing low-cost flow rate control into water hydraulic variable ballast system. Ocean Eng. 125:155–169. doi:10.1016/j.oceaneng.2016.08.001.